Photoelectron diffraction of twisted bilayer graphene

Sylvain Tricot, H. Ikeda, Hulerich Camel Tchouekem, Jc Le Breton, S. Yasuda, P. Krüger, Patrick Le Fèvre, D. Sébilleau, T. Jaouen, Philippe Schieffer

Photoelectron diffraction of twisted bilayer graphene

S. Tricot[a], H. Ikeda[b], H.-C. Tchouekem[a], J.-C. Le Breton[a], S. Yasuda[a], P. Krüger[b], P. Le Fèvre[a], D. Sébilleau[a], T. Jaouen[a,*], P. Schieffer[a]

[a] *Univ Rennes, CNRS, IPR (Institut de Physique de Rennes) - UMR 6251, F-35000, Rennes, France*
[b] *Graduate School of Engineering and Molecular Chirality Research Center, Chiba University, Chiba, 263-8522, Japan*

Abstract

Photoelectron diffraction (PED) is a powerful spectroscopic technique that combines elemental resolution with a high sensitivity to the local atomic arrangement at crystal surfaces, thus providing unique fingerprints of selected atomic sites in matter. Stimulated by the rapid innovation in the development of various analysis methods for probing the atomic and electronic structures of van der Waals (vdW) heterostructures of two-dimensional materials, we present a theoretical assessment of the capacity of PED for extracting structural properties such as stacking, twist angles and interlayer distances. We provide a complete description of PED for the benchmark vdW heterostructure bilayer graphene (BLG), by calculating and analyzing the PED of BLG in Bernal and AA-stacking as well as twisted BLG for a wide range of the twist angle.

Keywords: Photoelectron diffraction, full-multiple scattering, bilayer graphene, twist angles

1. Introduction

In the past few years, the remarkable progress in controlling the stacking of atomic sheets in van der Waals (vdW) heterostructures [1, 2] has opened up new avenues for manipulating electronic properties by moiré superlattices. In two-dimensional (2D) materials, a moiré superlattice can be formed by vertically stacking two layered materials with a twist angle that generally modifies the electronic band structure through umklapp scattering. At so-called "magic angle twist", low-energy flat subbands appear and electron interactions become the dominant energy scale, which may lead to emergent electronic phases, such as correlated insulators, superconductors, magnetism and topological electronic structures. In such a context, bilayer graphene (BLG) appears as the simplest vdW heterostructure that has demonstrated to exhibit correlated phases emerging from isolated flat bands upon small-angle twisting [3–8].

More recently, the observation of superconductivity and the quantum anomalous Hall effect in Bernal bilayers [9, 10] and the discovery of dodecagonal quasicrystalline order coexisting with Dirac fermions and enhancing interlayer coupling in 30°-twisted BLG [11, 12], showed that large twist angles BLG constitute a platform for exhibiting exotic physics as well. Whereas the moiré pattern of the dodecagonal quasicrystal is purely incommensurate with 12-fold rotational symmetry and no translational one, at twist angles satisfying the commensuration condition $\theta_t = \arccos \frac{3q^2-p^2}{3q^2+p^2}$ with p and q integers, twisted BLG forms spatially-periodic moiré pattern with a well-defined elementary unit cell. While the values $\theta_t = 0°$ and $\theta_t = 60°$ lead to the smallest possible unit cells with AA and Bernal (AB) stacking, twisted BLG with commensurate rotation angles θ_t and $60° - \theta_t$ appear as pairs leading to unit cells of equal areas but exhibiting distinct parities upon sublattice exchange (SE) [13, 14]. If the commensuration unit cell contains A and B sublattice sites in each layer coincident with atomic sites in the neigbouring layer, the SE parity is even with points having six-fold symmetry. It is odd with three-fold symmetry if only one sublattice site in the commensuration cell is eclipsed [14]. SE-even and SE-odd structures of a given commensuration pair are related by inter-layer lattice translation and can be deduced from the soustraction $q - p$ of the translation indices (p, q) that is a factor of 3 for even SE, only. Turning to the reciprocal space, the commensurate partners exhibit electronic band structures having the same symmetry as Bernal and AA-stacked BLG but with an interlayer coherence energy scale in the terahertz regime [15, 16]. As their untwisted parents, the coherent scattering between the Dirac cones of the two layers gives rise to an interface electronic structure exhibiting either massive Dirac bands, or a band gap supporting topological edge states [17, 18], depending on the SE parity.

To date, even if the increased sample quality hints at the possibility to experimentally emcompass the extremely rich physics of BLG from strongly-correlated electron phenomena at small twisted angles to quasicrystalline order and interlayer coherent coupling at larger ones, only few analysis methods allow for accurately accessing all together, the structural, physical and chemical properties of real stacking. In this context, photoelectron diffraction (PED) which exploits angle-resolved, core-level photoemission from a crystal surface, appears as very promising since it is element-specific and probes the *local* atomic structure around the emitting atoms at the Å length scale. In that paper, we examine the capability of PED for ac-

*Corresponding author
Email address: thomas.jaouen@univ-rennes.fr (T. Jaouen)

cessing local structural properties such as stacking, twist angles and interlayer distances of BLG by a comprehensive set of full-multiple scattering calculations. We first validate our theoretical procedure by confronting calculated PED patterns to existing experimental literature and demonstrate how sensitive PED is to the stacking geometry of BLG. Motivated by the experimentally observed layer-by-layer resolution of the C $1s$ core level for BLG when grown on SiC(0001) [19, 20], or transferred on SiO_2 [21–23], we also extract the PED stereographic plots for the bottom and top layers of BLG. We show that while the bottom layer PED provides information on the SE parity of the stacking, the top layer PED is similar to the one of single-layer graphene. This offers the unprecedented opportunity to determine the relative orientation of two stacked graphene layers and stacking arrangements of moiré patterns once twist angles are introduced. We then focus on twisted BLG for a wide range of rotation angles between the magic-angle and that of the dodecagonal quasicrystal ones, passing through various commensurate moiré crystals. We unveil three distinct regimes of PED associated with small, intermediate and large twisted-angles reflecting respectively the characteristic local Bernal and AA stacking of large moiré supercells, the SE-parities of the small-unit cell commensurate structures, and the 12-fold Stampfli tiling of the quasicrystal. Finally, through the energy-dependence of the normal-emission modulation function [24], we end up by illustrating the high sensitivity of PED to small variations of interlayer distances for both primitive and twisted BLG.

2. Computational details

Full multiple scattering spherical wave cluster calculations have been performed by using the MsSpec program [25–27]. The phase shifts have been calculated using the Hedin-Lundqvist exchange-correlation potential [28–30] whose imaginary part describes the finite photoelectron mean free path in the final state. The inner potential value in-between scattering centers was set to 12.5 eV. The polar angle (θ) is defined with respect to the surface normal and the azimuth angle (ϕ) with respect to the emission plane. The unpolarized photon source makes an angle of 45° with the electron analyzer direction. Both are fixed in the laboratory frame while the sample is rotated in (θ, ϕ). Lattice vibrations were described by averaging over T-matrix elements and using isotropic mean-square displacements fixed to 5×10^{-3} Å^2 [31]. In the calculated PED stereographic projections, the experimental resolution of the detector has been modeled by averaging photoelectron intensities over 13 directions evenly distributed in an acceptance cone with an angular aperture of 1.5°.

For each (θ, ϕ) direction, the total PED intensity results from the incoherent sum of the intensities associated with each inequivalent photoelectron emitter in the structure. In AA-, Bernal-stacked or twisted BLG, inequivalent emitters correspond to all carbon atoms contained in the supercell. A standalone multiple scattering calculation is run for each emitter, considering a set of approximately 400 atoms contained in a cylinder of 13 Å radius surrounding the emitter located on the cylinder's axis oriented along the [001] direction of the twisted BLG. This cluster geometry was carefully determined based on the convergence study with respect to the system size and the memory requirements needed for the calculation. Here we perform full multiple scattering calculations by matrix inversion rather than using a series expansion. This has the great advantage of solving the multiple scattering problem exactly. The downside is that the calculation requires a large amount of RAM which increases quickly with the number of atoms in the cluster N, and the maximum angular momentum $l_{\max}$ used to expand the photoelectron wavefunction in the spherical basis. The storage requirement is proportional to $[N \times (l_{\max} + 1)^2]^2$ with $l_{\max} \propto E^{1/2} r$ for kinetic energy E and atomic radius r. It is worth mentioning that the small size of a carbon atom makes it possible to keep $l_{\max}$ below a reasonable limit (< 15), enabling PED patterns to be computed in *full*-multiple scattering at energies as high as 650 eV. Since commensurate supercells considered in this study can contain as much as 11164 atoms, both process-based parallelism and standard shared memory loop-based parallelism of Lapack routines were used to make the most of computing power.

3. Results and discussion

3.1. PED sensitivity to BLG stacking: Experiment vs. full-multiple scattering simulations.

In order to demonstrate how powerful full-multiple scattering simulations are for accurately describing BLG, we first confront, in Fig. 1, calculated and experimental BLG PED data in stereographic projection. The experimental data are taken from Ref.[20] and were obtained for BLG grown on SiC(0001) by recording the photoemission intensity of the C $1s$ core level excited with a photon energy such that the kinetic energy of photoelectrons was 638.6 eV [Fig. 1a)]. The experimental PED data shows an overall hexagonal pattern and three-fold symmetry. The reduction from six- to threefold symmetry is evident both on the ring of intense spots at 45° [small white and light-grey circles on Fig. 1b)], and on the dark spots at ∼40° polar angles [large dark grey and dark circles on Fig. 1b)].

Nevertheless, the PED diagram also shows intense diffraction spots each 60° in ϕ at $\theta = 60°$ [white ellipses on Fig. 1b)], as well as dark hexagonal-shaped diffraction lines [dark, dark grey and grey hexagons on Fig. 1b)] of six-fold symmetry. Interestingly, both the bright diffraction spots and the dark diffraction lines are well reproduced in our calculations for the BLG with interlayer spacing 3.46 Å [1] regardless of whether Bernal [Fig. 1c)] or AA-stacking [Fig. 1d)] is assumed. These PED features are fingerprints of the honeycomb lattice of an isolated monolayer graphene and originate from purely in-plane scattering. Indeed, the very low atomic number of carbon, its small scattering power and the large interlayer separation characteristic of layered materials implies that in-plane coherent scattering is

[1] Note that we did not attempt to optimize the calculation parameters for improving the experiment-theory agreement since that work was already well done in Ref. [20].

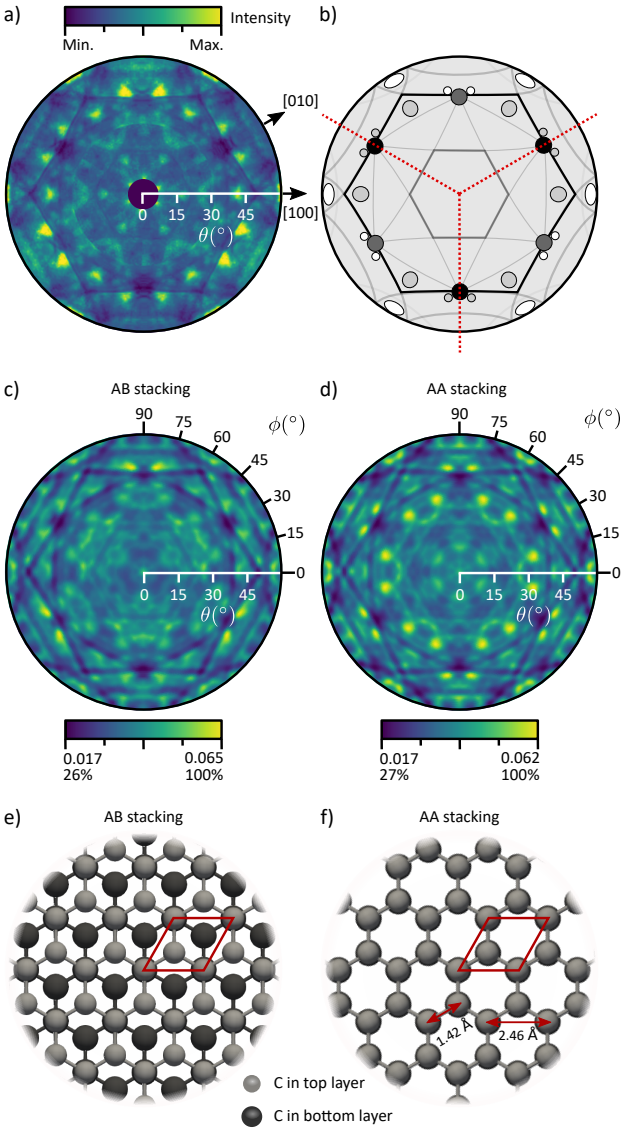

Figure 1: [color online] a) Stereographic projection of PED data of the C 1*s* core level at 638.6 eV kinetic energy (taken from [20]). b) Sketch of the main features found in the diffraction pattern. Red dashed lines highlight the three-fold symmetry. c)-d) Full-multiple scattering calculations of the stereographic projection of PED from C 1*s* at 638.6 eV kinetic energy for a Bernal(AB)- c) and AA-stacked d) BLG. The calculations used the same experimental geometry as a). e)-f) Top views of the two superimposed C honeycomb lattices for Bernal (AB) e), and AA-stacked BLG f). The primitive cells of the Bernal and AA stacking having either half, or all of the sublattices sites eclipsed are highlighted in red on e) and f). Are also indicated on f) the C-C nearest neighbour distance (1.42 Å) and the length of the basis vectors of the graphene unit cell (2.46 Å).

much larger than out-of-plane scattering [31, 32]. In particular, the sharp hexagonal-shaped dark diffraction lines are reminiscent of destructively overlapping circular diffraction rings [33] already observed in graphite as well as boron nitride [34–36], and appearing around the forward-focusing peaks associated with in-plane single scattering by C atoms of successive coordination shells around the emitter. The opening angles of the associated interference cones depend on the emitter-scatterer distance, the photoelectron wavenumber, and the scattering phase shift which is particularly significant for an *s*-wave on carbon at this kinetic energy [35]. A complete description of these diffraction rings is beyond the scope of the present paper and has been already done elsewhere. Nevertheless, our simulations performed for a graphene layer have confirmed that they can be well reproduced at the single-scattering level considering eight coordination shells (that corresponds to an emitter scatterer distance of 5.12 Å) around the carbon emitter (results not shown). For the purpose of the present paper, we keep in mind that these peculiar PED features are all associated with interference of the direct electronic wave with those single-scattered along the dense C-C atomic directions of the six-fold symmetric graphene lattice.

We now focus on PED features that carry information about the stacking geometry. Specifically we look at the signal from electrons photoemitted from a bottom layer C atom and scattered by a top layer atom. We see that the simulated PED stereographic projection of the Bernal-stacked BLG exhibits a clear three-fold symmetry [Fig. 1c)], whereas the one of the AA stacking [Fig. 1d)] shows bright sixfold-symmetric diffraction spots at $\theta = 32.5°$ that do not appear in experiment. This is fully consistent with the SE-odd, respectively SE-even parities of the Bernal and AA stacking of BLG whose unit cells have either half [Fig. 1e)], or all [Fig. 1f)] of the sublattices sites eclipsed. It turns out that, even if in-plane single scattering clearly dominates at this kinetic energy, the BLG stacking sequence can clearly be distinguished by looking at the PED pattern. The only experimental features that are not captured in the simulated PED stereographic projection of Bernal-stacked BLG are the six-fold symmetric bright spots at $\theta = 17.6°$. They are most likely due to the trilayer stacking made of Bernal BLG and the carbon buffer layer when grown on the SiC(0001) substrate. We conclude from this section that PED of BLG with a kinetic energy as high as ~640 eV, can be reproduced accurately and with a high sensitivity to the stacking geometry with the present full-multiple scattering simulations.

3.2. Layer-resolved PED of AA-stacked BLG.

We now focus on the separated contributions of each layer to the total PED pattern of AA-stacked BLG. Layer resolution is a trivial problem from a theoretical point of view, since in core-level PED the photoemission intensities of different emitter atoms add incoherently. In experiment, layer resolution can be achieved by numerical deconvolution of core levels exhibiting well-defined chemical shifts. It has been reported for BLG grown on SiC(0001) [19, 20], or transferred on SiO_2 [21–23]. Figure 2a) shows the PED stereographic projection of AA-stacked BLG calculated at the single-scattering level. Single scattering calculations greatly reduce computation time while preserving the main features of the full mulitple scattering result [Fig. 1d)]. Indeed, both the hexagonal-shaped dark diffraction lines characteristic of single-layer graphene at large polar angles and the distinguishing features of the AA-stacking at smaller angles are well reproduced in the single-scattering calculation [Fig. 2a)]. In particular, the bright sixfold-symmetric diffraction spots at $\theta = 32.5°$ can be interpreted as belonging to the sides of typical volcano-shaped PED

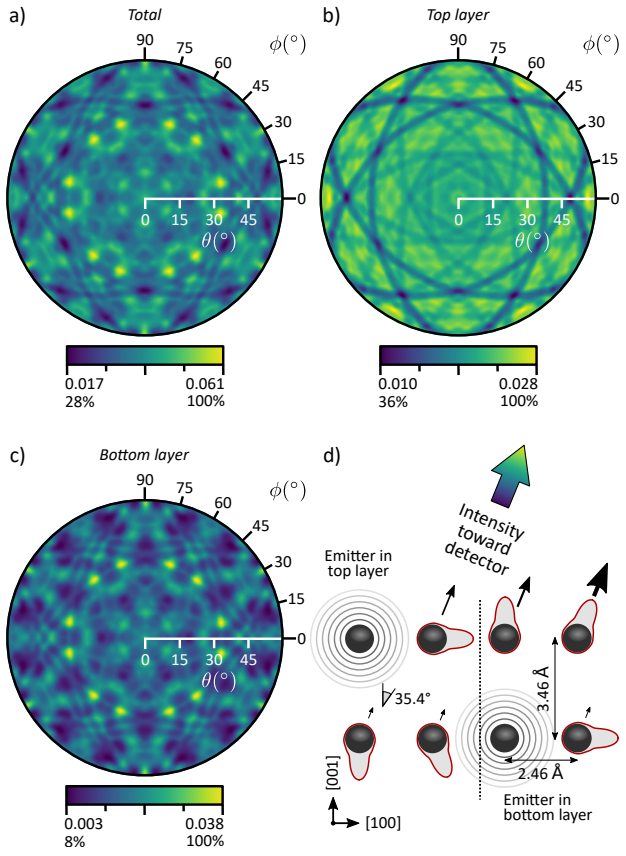

Figure 2: [color online] a) Single-scattering calculation of the stereographic projection of PED from C 1s at 638.6 eV kinetic energy for AA-stacked BLG. b),c) Corresponding stereographic projections of PED for the top and bottom layers of the stacking, respectively. d) Sketch of first nearest neighbors atoms in the $\{\bar{1}20\}$ planes showing dominant scattering paths, as indicated by the size of the black arrows, for inter- and intra-layer scattering. The scattering factors calculated at 638.6 eV kinetic energy are plotted in red. The detector direction is fixed along the interlayer forward focusing direction at θ =35.4°.

structures centered around the interlayer forward focusing direction at θ =35.4°. As explained for other systems, this volcano shape is strongly energy-dependent and emerges from interference phenomena due to atoms close to dense forward scattering directions [24, 37–39].

The layer-resolved PED stereographic projections of the top [Fig. 2b)] and bottom [Fig. 2c)] layers of the AA-stacked BLG, now allow us to show that the full information about the stacking geometry is brought by PED from the bottom layer only, the PED pattern of the top layer being almost identical to the one of an isolated single layer graphene (result not shown). In contrast to the PED pattern of the bottom layer which is dominated by inter-layer forward scattering events, the PED pattern of the top layer is almost purely constructed from interfering in-plane single scattering events. Indeed, considering an emitter atom in the top layer, the scattering paths carrying information about the stacking geometry of BLG have to imply out-of-plane backscattering on the bottom layer for allowing the photoelectrons to be detected. So, even though such scattering paths do exist, one can understand, by looking at the scattering factor which is rather forward-peaked at this kinetic energy, that these back-scattering events have negligible intensity compared to the intra-layer scattering [Fig. 2d), left-hand side]. In contrast, the probability for an electron photoemitted from the bottom layer to suffer only one scattering process on a top-layer atom before reaching the detector is much larger than the probability for this electron to undergo an additional in-plane scattering event [see the Fig. 2d), right-hand side].

Our layer-resolved study thus highlights drastically different PED patterns for the bottom and top layers of BLG, the former providing information on the SE parity of the stacking and the latter being similar to single-layer graphene. As we will now see in the next sections by introducing twist angles, this not only offers an appealing way for accurately determining the relative orientations of two stacked graphene layers, but also for resolving the internal atomic arrangement of moiré patterns on the entire possible range of twisted angles, from small magic angles up to the 30°-twisted quasicrystal.

3.3. Twisted BLG.

We start by demonstrating that introducing rotational misalignment between the two layers of BLG, while working in the forward-scattering regime of PED, completely modifies the PED pattern of the bottom layer and allows a precise determination of the twist angle. First of all, we constructed a twisted BLG structure at 21.79° commensurate angle corresponding to translation indices $(p, q) = (1, 2)$ and giving rise to the smallest commensurate hexagonal Moiré supercell with a 6.51 Å basis vector length and containing 28 atoms [see Table 1]. To do so, we considered the perfectly eclipsed honeycomb lattices of the AA-stacked BLG and rotated counter-clockwise the top layer around coinciding carbon atoms of the two graphene sublattices.

Figures 3a)-b) show the layer-resolved single scattering-calculated stereographic projections of PED from C 1s at 638.6 eV kinetic energy for the twisted BLG. While the PED of the top layer [Fig. 3a)] is identical to the PED stereographic projection of the top layer of the AA-stacked BLG [Fig. 2b)], i.e. of single layer graphene (apart a rotation corresponding to the introduced twist angle since referenced to the bottom layer), we immediately see that the bottom layer of twisted BLG now exhibits a drastically different PED pattern from its AA-stacked counterpart [Fig. 2c)]. All the PED features characteristic of interlayer forward scattering have disappeared and the PED pattern is similar to that of the top layer of twisted BLG [Fig. 3a)], except for more blurred diffraction lines and a global rotational misalignment.

In fact, due the multiplicity of atomic environments and associated upward scattering directions around the emitting atom resulting from the twist, the total PED intensity signal that was before concentrated around well-defined dense forward-scattering directions becomes redistributed among many polar and azimuthal angles leading to a strongly reduced PED anisotropy over the full stereographic projection. As a result, the in-plane single forward-scattering events that hardly contribute to the total PED intensity in a simple stacking geometry, become important and dictate the PED anisotropy in twisted BLG. Interestingly, this crossover from dominant inter-

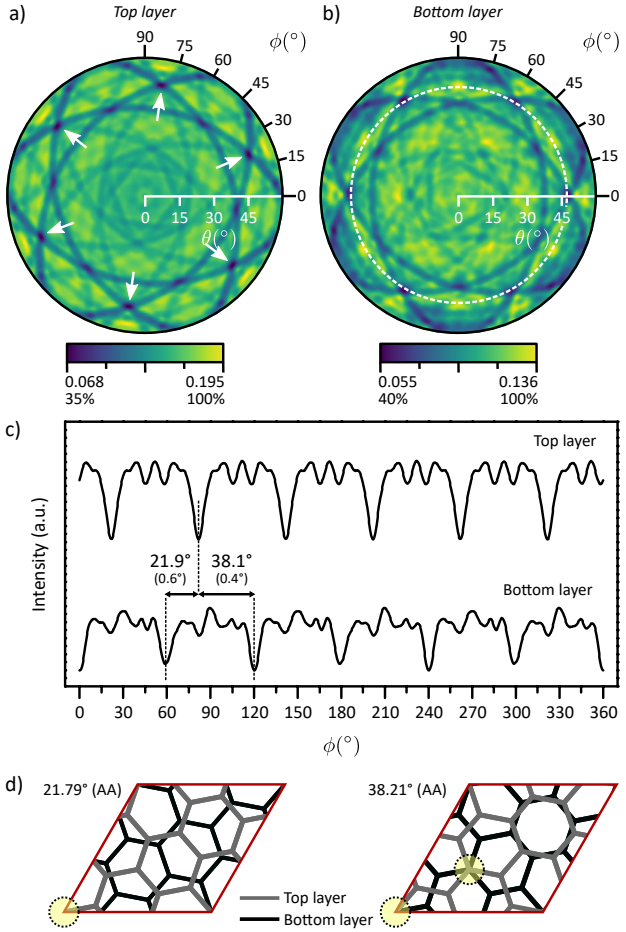

Figure 3: [color online] a,b) Layer-resolved single scattering-calculated stereographic projections of PED from C 1s at 638.6 eV kinetic energy for a twisted BLG at 21.79° commensurate angle. c) Azimuthal profiles for top and bottom layers at 47.5° polar angle [see the white-dashed circle in b)]. The white arrows in a) indicate the PED intensity depressions appearing at the crossing points of the hexagonal black diffraction lines. They are manifested as six sharp inverted peaks in the azimuthal PED profiles in c) and are used as reference for the twist angle determination (standard deviation in parentheses). d) Twisted BLG supercells of 21.78° and 38.21° commensuration partners. Whereas the unit cells are of equal areas they exhibit distinct SE parities as highlighted by the yellow circles that shows the coincident sublattice sites. One sublattice site is eclipsed in SE-odd commensuration cell (21.78°, starting from AA stacking). Both A and B sublattice sites of each layer coincide with atomic sites of the neigbouring layer in SE-even commensuration cell (38.21°, starting from AA stacking).

to intra-layer forward scattering regime concomitantly offers an appealing experimental way to determine misorientation angles of twisted BLG in high-energy PED since the PED patterns of the top and bottom layers are both characteristic of an isolated single layer graphene and differ essentially only by a relative rotation. Figure 3c) shows azimuthal PED profiles taken for both the top and bottom layers at fixed polar angle value of 47.5° [white-dashed circle in Fig. 3b)]. This polar angle was chosen because it allows to focus on the PED intensity depressions appearing at the crossing points of the hexagonal black diffraction lines [see white arrows in Fig. 3a)]. They show up as six sharp inverted peaks in the azimuthal PED profiles [Fig. 3c)], providing an ideal spectroscopic fingerprint to access the twist angle value with a reasonable precision. Indeed, the inverted peaks of the azimuthal PED profile of one given layer always appear at 21.9°±0.6° and 38.1°±0.4° from two consecutive ones of the other layer. These two angle values in fact correspond to the commensuration partners θ_t and $60^\circ - \theta_t$ that lead to unit cells of equal areas but exhibit distinct SE parities [13, 14] [see Fig. 3d)]. Interestingly, the three-fold symmetry of our computed SE-odd BLG twisted stacking with translation indices $(p, q) = (1, 2)$ is also tracked in the PED of the bottom layer. Whereas the top layer exhibits a PED stereographic projection identical to the one of single layer graphene and inverted peaks of equal amplitude in the azimuthal profile, the PED stereographic projection of the bottom layer shows a slight 60°-anisotropy of the intensity at small polar angles ($\theta \leq 30^\circ$) [Fig. 3b)], and the azimuthal profile exhibits inverted peaks of equal amplitude every 120°, only [bottom profile, Fig. 3c)].

Having demonstrated that layer-resolved high-energy PED is a particularly well-suited experimental technique for accessing both twist angle values and SE parities of moiré supercells in BLG, let us now go a step further and see if PED also yields structural information about the internal atomic arrangements of the moiré patterns themselves. To this end, we now focus on low-energy PED by working at 100 eV kinetic energy within the full-multiple scattering approach. Indeed, at such low kinetic energy, the scattering factor is more isotropic and the single-scattering approximation is no longer sufficient. Together with the extremely short inelastic mean free path of photoelectrons (5.8 Å) which prevents the formation of well-defined diffraction fringes, one enters in an ideal PED regime for obtaining structural information about the atomic configurations within the moiré supercells. Furthermore, working at such a low kinetic energy allows us to explore a large number of calculation parameters and atoms in the cluster with reasonable computation times and limited memory resources (≤100 GB), which is crucial for large moiré supercells. Figure 4 shows the full-multiple scattering calculated PED stereographic projections of the BLG bottom layer from C 1s at 100 eV kinetic energy for various moiré supercells within a twist angles range

θ_t (°)	p	q	N	$\|\|\vec{t_i}\|\|$ (Å)
0.00	1	1	4	2.46
1.08	30	31	11164	129.96
3.89	8	9	868	36.24
4.41	7	8	676	31.98
13.17	2	3	76	10.72
16.43	3	5	196	17.22
17.90	4	7	124	13.70
21.79	1	2	28	6.51
25.04	4	9	532	28.37
26.01	3	7	316	31.98
27.80	2	5	52	8.87

Table 1: Selected commensurate angles θ_t in a 30°-wide interval of twist angles. (p, q), N, and $\|\|\vec{t_i}\|\|$ are the translation indices, number of atoms and length of the primitive translation $\vec{t_i}$ of the associated commensuration supercell.

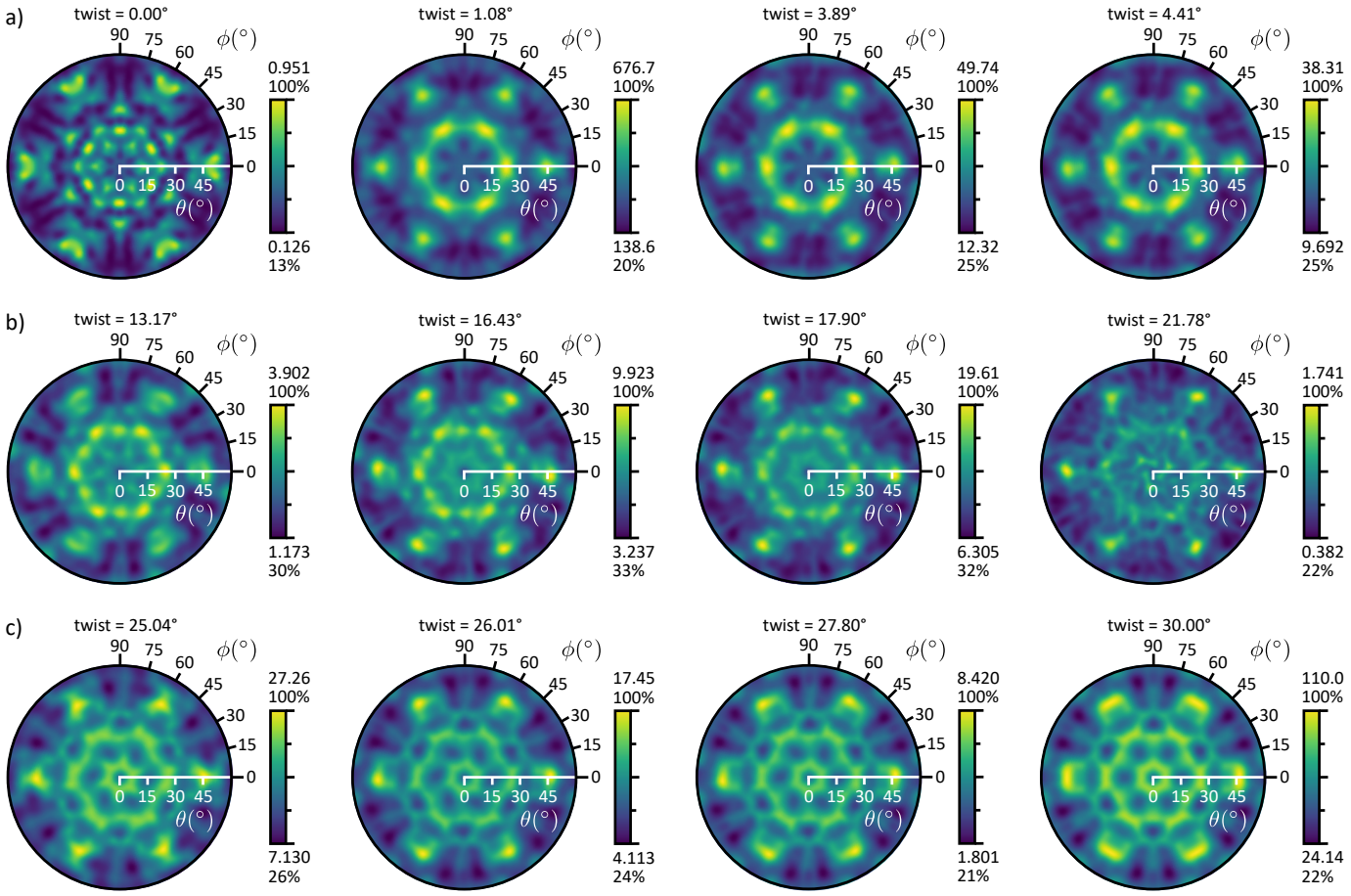

Figure 4: [color online] Bottom layer stereographic projections of PED from C 1s at 100 eV kinetic energy of twisted BLG calculated in full multiple scattering. Three distinct regimes are observed depending on the twist angles: a) small angles regime from 0° (AA stacking) to 4.41°, b) Moiré crystal regime from 13.17° to 21.78° and c) quasicrystal regime from 25.04° to 30.00°.

of 30° [see Table 1] [2]. We are mostly interested in twist angles that lead to small commensurate supercells, but for the sake of completeness with regard to the rich physics of twisted BLG, we consider two more strutures: (i) one with θ_t=1.08°, corresponding to the magic angle [3], which gives rise to a supercell containing as many as 11164 atoms [Fig. 4a), second panel], and (ii) the purely incommensurate dodecagonal quasi-crystal with θ_t=30° [Fig. 4c), last panel]. As before, at large polar angles ($\theta \geq 30°$), all PED patterns share many similar features, which may be attributed to in-plane multiple scattering events and which are inherited from single layer graphene (result not shown). At small polar angles ($\theta \leq 30°$), however, one can indentify three types of closely resembling PED patterns associated with small [Fig. 4a)], intermediate [Fig. 4b)] and large twisted angles [Fig. 4c)]. At small twist angles, all PED patterns exhibit a six-fold symmetry and rather broad bright spots lying on diffuse ring of intensity each 60° in ϕ at $\theta = 22.3°$. In contrast, the pattern for intermediate twist angles have six- or three-fold symmetry [see e.g. Fig. 4b), last panel] and show PED spots which are more structured and resolved from the diffuse intensity ring as reminiscent of the sharp PED features of the AA-stacked BLG [Fig. 4a), first panel]. Last, for the largest twist angles, a rather diffuse and robust honeycomb-like PED pattern is always found [Fig. 4c)].

Let us now discuss these three identified PED regimes in terms of internal atomic arrangements of moiré superlattices. Figure 5a) shows the moiré supercell of BLG (red parallelogram) generated by the magic-twist angle ($p = 30, q = 31$). The atomic registry within such a large-period superlattice (~13 nm) can be viewed as evolving smoothly between widely separated regions with locally AB, BA, AA and SP (saddle point) stackings. This is typical of superlattices described by a small twist. The larger the twist angle, the smaller the superlattice period and total area proportion of atoms belonging to a well-defined stacking. Figure 5b) shows a full-multiple scattering calculated PED stereographic projection corresponding to the incoherent sum of PED patterns associated with AA, AB, BA and SP stackings, only. Interestingly, it closely matches the PED patterns obtained for small twist angles [Fig. 4a)] by considering all the inequivalent emitter atoms of the supercells. Both the six-fold

[2] Note that we will not discuss the top layer of BLG anymore. Indeed, at low kinetic energy, even though the top layer PED pattern is constructed from multiple scattering events that are more isotropic in space, non stacking-sensitive in-plane multiple scattering remains much more dominant.

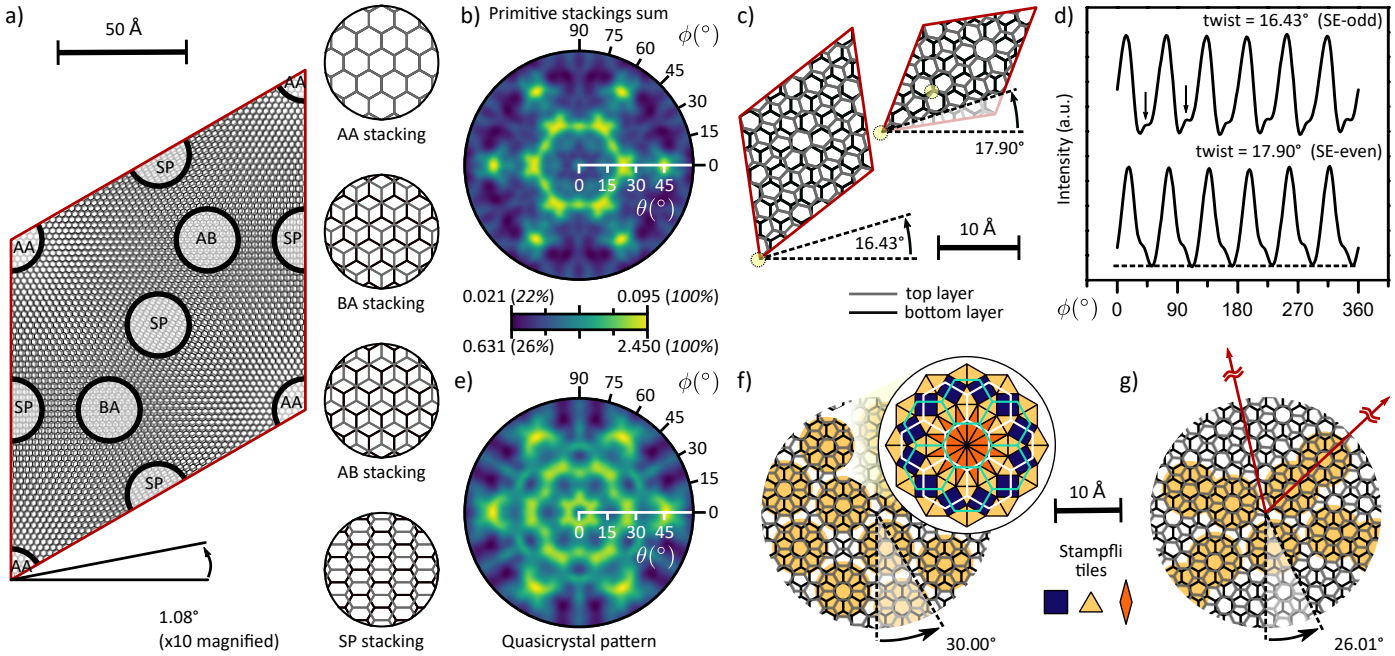

Figure 5: [color online] a) Moiré supercell of BLG (red parallelogram) generated by the magic-twist angle (p = 30, q = 31). The atomic registry within such a large-period superlattice (~13 nm) can be viewed as evolving smoothly between widely separated regions with locally AB, BA, AA and SP stackings. b) Full-multiple scattering calculated PED stereographic projection from C 1s at 100 eV kinetic energy corresponding to the incoherent sum of PED patterns associated with AA, AB, BA and SP stackings. c) Twisted BLG supercells of SE-odd and SE-even commensurate moiré crystals at 16.43° (p = 3, q = 5) and 17.90° (p = 4, q = 7) of twist angle. The yellow areas highlight coincident sublattice sites. Whereas only one sublattice site is eclipsed in SE-odd commensuration cell, both A and B sublattice sites of each layer coincide with atomic sites of the neigbouring layer in SE-even commensuration cell. d) Integrated azimuthal profiles from 0° to 15° in polar angle for 16.43° (top) and 17.90° (bottom) twisted BLG evidencing the sensitivity to the SE parity. e) Full-multiple scattering calculated PED stereographic projection from C 1s at 100 eV kinetic energy of the characteristic tiling located at the center of rotation in the Stampfli tessellation of the 12-fold quasicrystal. f-g) Twisted BLG superlattices of the dodecagonal quasicrystal and of a large commensurate moiré crystal at 30.00° and 26.01° (p = 3, q = 7) of twist angle, respectively. The orange areas in f) and g) highlight the 48-atoms subset of the Stampfli tessellation considered in the calculation of e).

symmetry and bright spots lying on the diffuse ring of intensity at θ = 22.3° are well reproduced. While the former can be understood as emerging from the mixed six-fold, three-fold with mirror plane and two-fold symmetries of 120° equivalent domains of the AA, AB/BA and SP stackings respectively, the latter corresponds to the out-of-plane nearest neighbors forward scattering atomic direction existing in all primitive BLG stackings. This demonstrates, that, for such a range of twist angles, the whole structural information about the atomic arrangement within the moiré superlattice is contained within small clusters of atoms belonging to stackings very close to those of primitive BLG. While this offers appealing computational means for drastically reducing the memory ressources when performing full-multiple scattering simulations of small twist angles superlattices, it also demonstrates that low-energy PED will not show a high sensitivity to the twist angle as long as these structures do not correspond to commensurate moiré crystals of specific atomic configurations and SE parities. Figure 5c) shows twisted BLG supercells of SE-odd and SE-even commensurate moiré crystals at twist angles 16.43° and 17.90°, respectively. For such close θ_t values associated with rather large supercells, we can see that, although the PED patterns look very similar [Fig. 4b)], they do carry information about the SE parity. Indeed, the extracted azimuthal profiles integrated from 0° to 15° in polar angle exhibit slight shoulders on the left-hand side of the main PED peaks of either 120° [top azimuthal profile, Fig. 5d)] or 60° [bottom azimuthal profile, Fig. 5d)] periodicity as expected for the odd and even SE parities of the commensurate moiré crystals associated with the translation indices (p, q)= (3, 5) and (4, 7), respectively.

Note that the sensitivity to the SE parity in this intermediate range of twist angles strongly depends on the size of the commensurate moiré supercell. As we can see on Fig. 4b), the three-fold symmetry of the smallest SE-odd moiré supercell for a twist angle of 21.78°, is easily tracked over the first 30° of the PED stereographic projection without the need for a highly-resolved azimuthal profile. In this commensurate moiré supercell, the emitter atom that carries the SE-odd parity counts for 1/14 of the full PED signal which, apart for the Bernal-stacked BLG, is the highest achievable intensity ratio.

Turning now to larger twist angles, we saw that we quickly entered in the PED regime dictated by a robust honeycomb-like PED pattern. Similar to the stacking analysis that we performed for the small twist angles, we can show that such a peculiar pattern arises from the specific atomic configuration of the 12-fold Stampfli tiling of the BLG quasicrystal. Figure 5e) shows a PED stereographic projection calculated considering only a 48-atoms subset of the characteristic tiling located at the center of rotation in the Stampfli tessellation [see Fig.5f)] [40]. It almost perfectly matches not only the full-multiple scattering calculation of the 30°-twisted BLG [last panel, Fig. 4c)] but also the PED pattern calculated for the whole considered range of

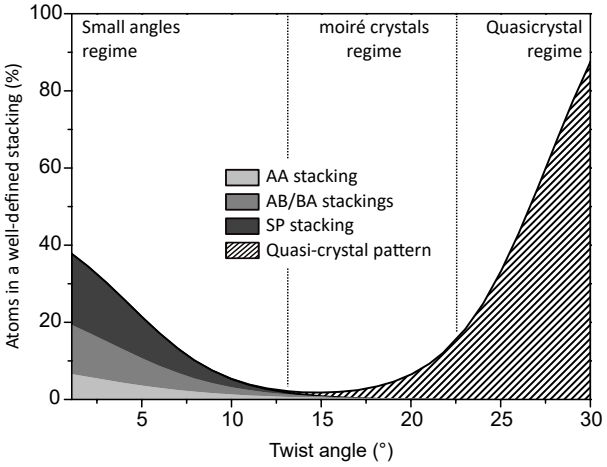

Figure 6: PED phase diagram of twisted BLG: proportion of atoms belonging in a well-defined stackings of either primitive BLG [Fig. 5a)] or Stampli tessellation of BLG quasi-crystal [Fig. 5f)] as a function of commensurate twist angles from 1° to 30°. The boundaries of the various regimes well correspond to those identified in Fig. 4.

large twist angles. This demonstrates that the honeycomb-like PED pattern directly reflects the ubiquity of atomic arrangements closely matching the one of the 12-fold Stampfli tiling as seen in Fig.5g). It is also worth mentioning that even if the quasi-crystal lacks translational symmetry, its rotational symmetry as well as its fractal nature allows to restrict PED calculations to small clusters of atoms containing the elementary building block of the Stamplfi tessellation and of diameter roughly corresponding to the inelastic mean free path. We close this section by summarizing our results in a *PED phase diagram of twisted BLG* [Fig. 6]. It is based on the proportion of atoms belonging to a well-defined stacking of either primitive BLG or Stampli tessellation of BLG quasi-crystal as a function of the twist angle. To do so, we first consider each emitter as well as its three first neighbors in the same layer. We then consider a local AA stacking if, for these four atoms, one lies above another one of the other layer within a tolerance radius corresponding to half the atomic radius of carbon (r_t = 0.35 Å). For accounting for the AB/BA and SP stackings, one simply applies the translation needed to recover an AA stacking before checking the interlayer atomic coincidence. By applying this procedure, an atom is either identified as AA, AB/BA, SP or none of the three, but never falls into more than one of these categories. For the stacking characteristic of the quasi-crystal, we consider 24 atoms of the pattern identified in figure 5f) centered on the hexagon to which the emitter atom belongs to and rotate them by 30° before testing if all of these 24 atoms can match their in-plane position with 24 atoms of the second layer using the same tolerance criterion as above. Figure 6 shows the so-obtained PED phase diagram of twisted BLG. It validates the tolerance criterion we applied since it very well tracks the three PED regimes that we have identified above: a *magic-angle like regime* at small twist angles ($0° \leq \theta_t \leq 13°$) where PED tracks the proportion areas of relatively well-defined AA, AB, BA and SP stackings, *a moiré crystal regime* at intermediate twist angles ($13° \leq \theta_t \leq 23°$) in which the SE-parities of the commensurate moiré supercells are probed and a *moiré quasi-crystal regime* at large twist angles ($23° \leq \theta_t \leq 30°$) that reflects the characteristic tiling of the 12-fold Stampfli tessellation.

3.4. Sensitivity of modulation functions to interlayer distances of primitive and twisted BLG.

In this last section, we illustrate how sensitive the energy-dependence of the modulation function of the C 1*s* cross-section is to tiny changes of the interlayer distance in both primitive and twisted BLG. We consider the modulation function at normal-emission (θ = 0°), calculated in full-multiple scattering for kinetic energies of photoelectrons ranging from 50 to 250 eV, i.e., in the low-energy backscattering regime of PED [41, 42]. The modulation function $\chi(E)$ is defined by [24]:

$$\chi(E) = \frac{I_0(E) - I_{0,direct}(E)}{I_{0,direct}(E)}, \quad (1)$$

where $I_0(E)$ and $I_{0,direct}$ are respectively the calculated, total and direct (diffraction-free), normal photoemission intensities at a given kinetic energy E. Figure 7a) shows the modulation functions of the top (red curve, $\chi_{top}(E)$) and bottom (black curve, $\chi_{bottom}(E)$) layers of AA-stacked BLG as well as the one of single layer graphene (black-dashed curve) for comparison. All the modulation functions show an oscillating behavior that arises from coherent interference phenomena of different scattering paths, the relative phases changing due to the varying electron wavelength, and positive (negative) values of $\chi(E)$ corresponding to purely constructive (destructive) interference. For single layer graphene, where all interference is due to in-plane scattering, $\chi(E)$ exhibits a long-period oscillation of ~130 eV corresponding to the graphene lattice parameter of 1.42 Å in real-space. Focusing on BLG, we first see that the in-plane nearest-neighbors forward scattering events that give rise to the long-period oscillation still contribute to $\chi_{bottom}(E)$ and $\chi_{top}(E)$ as a broad background. Yet, they both show additional modulations of smaller periods reflecting out-of-plane scattering events. While $\chi_{bottom}(E)$ results from the combination of one main modulation of frequency ~60 eV with a secondary one of half period, $\chi_{top}(E)$ is made of one single frequency of ~30 eV superimposed to the in-plane long-period oscillation. When these kinetic energy oscillation frequencies are transposed to real-space, they correspond to the interlayer distance (3.46 Å) for the 60 eV period and twice the interlayer distance (7.92 Å) for 30 eV. In fact, for the top layer, the normal-emission configuration only selects the 180° backscattering geometry resulting in a modulation function dominated by a single oscillation of frequency corresponding to twice the value of the inter-layer distance [42]. For the bottom layer, it also takes into account the favorable out-of-plane forward scattering carrying the path difference associated to one vdW gap. Figure 7b) shows a zoom-in of $\chi_{top}(E)$ around the modulation peak at ~175 eV for various interlayer distance of the AA-stacked BLG in a range of ±0.2 Å around 3.46 Å. We see that the modulation peak experiences rather large negative or positive energy shifts for increased or

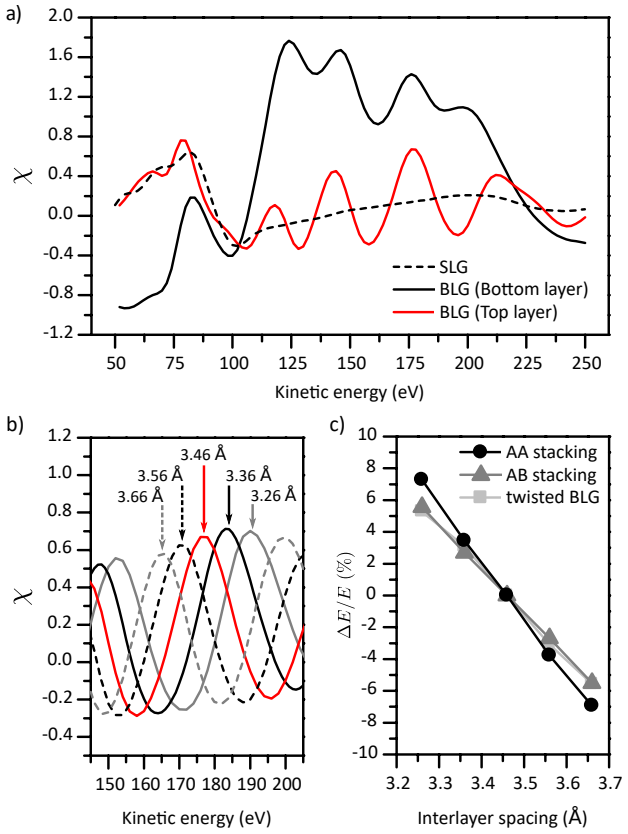

Figure 7: [color online] a) C 1s normal-emission modulation function as a function of kinetic energy of the top (red curve, $\chi_{top}(E)$) and bottom (black curve, $\chi_{bottom}(E)$) layers of AA-stacked and of single layer graphene (black dashed curve). b) Zoom-in of $\chi_{top}(E)$ around the modulation peak at ~175 eV for various interlayer distance in a range of ±0.2 Å around 3.46 Å. c) Relative energy shifts of modulation maxima of $\chi_{top}(E)$ as a function of the interlayer distances for AA (black circles), Bernal (dark grey triangles), and 21.8°-twisted BLG (light grey squares).

decreased interlayer distances, respectively. The relative energy shift $\Delta E/E$ of the modulation peak depends almost linearly on the interlayer spacing [dark curve with circles on Fig. 7c)], with a slope of about 40 %/Å demonstrating the remarkable sensitivity of backscattering energy-scans to small changes of the interlayer distances. This applies not only to primitive BLG, where the modulation function of the top layer of the Bernal-stacking shows identical dependence on the interlayer distance [heavy-grey curve with triangles on Fig. 7c)], but also to twisted BLG as demonstrated for the 21.79°-twisted commensurate BLG supercell [light-grey curve with squares on Fig. 7c)].

4. Conclusion

By theoretically analyzing the PED pattern formation of twisted BLG with single- and multiple scattering calculations, we have thoroughly examined the capacity of PED for accessing, at the sub-Å length scale, local structural properties of moiré superlattices made of twisted vdW materials. We have shown that high-energy PED can be used for determining both twist angle values and SE parities of moiré supercells, whereas low-energy PED allows to obtain structural information about the internal atomic arrangements of the moiré superstructures and to probe interlayer distances in energy-scan mode. We hope that these theoretical findings will motivate experimentalists to perform PED with high angle, energy and spatial resolution for deeply probing the atomic structure of the vast and fascinating family of twisted, strained, and intercalated vdW materials.

CRediT authorship contribution statement

S. Tricot: Writing-review editing, Methodology, Investigation, Formal analysis, Supervision, Resources, Data curation, Software. **H. IKeda**: Investigation, Review editing. **H.-C. Tchouekem**: Investigation, Review editing. **J.-C. Le Breton**: Investigation, Review editing. **S. Yasuda**: Investigation, Review editing. **P. Krüger**: Investigation, Writing-review editing, Supervision. **P. Le Fèvre**: Investigation, Writing-review editing. **D. Sébilleau**: Project administration, Software, Review editing. **T. Jaouen**: Writing – review editing, Writing – original draft, Methodology, Investigation, Formal analysis, Supervision. **P. Schieffer**: Project administration, Supervision, Methodology, Resources, Investigation, Formal analysis.

Declaration of Competing Interest

The authors declare that there are no known conflicts of interest and no significant financial support associated with this work that could have influenced its outcome.

Data availability

Data will be made available on request.

Acknowledgments

S. Tricot, J.-C. Le Breton, D. Sébilleau, T. Jaouen and P. Schieffer acknowledge partial funding from Horizon Europe MSCA Doctoral network grant n.101073486, EU-SpecLab, funded by the European Union. H.-C. Tchouekem and T. Jaouen acknowledge the support of the French National Research Agency (ANR) (MOSAICS project, ANR-22-CE30-0008). All the authors thank J. Gardais and G. Raffy for their technical support on the computing cluster.

References

[1] K. Kim, M. Yankowitz, B. Fallahazad, S. Kang, H. C. P. Movva, S. Huang, S. Larentis, C. M. Corbet, T. Taniguchi, K. Watanabe, S. K. Banerjee, B. J. LeRoy, E. Tutuc, van der Waals Heterostructures with High Accuracy Rotational Alignment, Nano Letters 16 (3) (2016) 1989–1995.

[2] R. Ribeiro-Palau, C. Zhang, K. Watanabe, T. Taniguchi, J. Hone, C. R. Dean, Twistable electronics with dynamically rotatable heterostructures, Science 361 (6403) (2018) 690–693.

[3] Y. Cao, V. Fatemi, S. Fang, K. Watanabe, T. Taniguchi, E. Kaxiras, P. Jarillo-Herrero, Unconventional superconductivity in magic-angle graphene superlattices, Nature 556 (7699) (2018) 43–50.

[4] Y. Cao, V. Fatemi, A. Demir, S. Fang, S. L. Tomarken, J. Y. Luo, J. D. Sanchez-Yamagishi, K. Watanabe, T. Taniguchi, E. Kaxiras, R. C. Ashoori, P. Jarillo-Herrero, Correlated insulator behaviour at half-filling in magic-angle graphene superlattices, Nature 556 (7699) (2018) 80–84.

[5] M. Yankowitz, S. Chen, H. Polshyn, Y. Zhang, K. Watanabe, T. Taniguchi, D. Graf, A. F. Young, C. R. Dean, Tuning superconductivity in twisted bilayer graphene, Science 363 (6431) (2019) 1059–1064.

[6] A. L. Sharpe, E. J. Fox, A. W. Barnard, J. Finney, K. Watanabe, T. Taniguchi, M. A. Kastner, D. Goldhaber-Gordon, Emergent ferromagnetism near three-quarters filling in twisted bilayer graphene, Science 365 (6453) (2019) 605–608.

[7] X. Lu, P. Stepanov, W. Yang, M. Xie, M. A. Aamir, I. Das, C. Urgell, K. Watanabe, T. Taniguchi, G. Zhang, A. Bachtold, A. H. MacDonald, D. K. Efetov, Superconductors, orbital magnets and correlated states in magic-angle bilayer graphene, Nature 574 (7780) (2019) 653–657.

[8] M. Serlin, C. L. Tschirhart, H. Polshyn, Y. Zhang, J. Zhu, K. Watanabe, T. Taniguchi, L. Balents, A. F. Young, Intrinsic quantized anomalous Hall effect in a moiré heterostructure, Science 367 (6480) (2020) 900–903.

[9] H. Zhou, L. Holleis, Y. Saito, L. Cohen, W. Huynh, C. L. Patterson, F. Yang, T. Taniguchi, K. Watanabe, A. F. Young, Isospin magnetism and spin-polarized superconductivity in Bernal bilayer graphene, Science 375 (6582) (2022) 774–778.

[10] F. R. Geisenhof, F. Winterer, A. M. Seiler, J. Lenz, T. Xu, F. Zhang, R. T. Weitz, Quantum anomalous Hall octet driven by orbital magnetism in bilayer graphene, Nature 598 (7879) (2021) 53–58.

[11] S. J. Ahn, P. Moon, T.-H. Kim, H.-W. Kim, H.-C. Shin, E. H. Kim, H. W. Cha, S.-J. Kahng, P. Kim, M. Koshino, Y.-W. Son, C.-W. Yang, J. R. Ahn, Dirac electrons in a dodecagonal graphene quasicrystal, Science 361 (6404) (2018) 782–786.

[12] W. Yao, E. Wang, C. Bao, Y. Zhang, K. Zhang, K. Bao, C. K. Chan, C. Chen, J. Avila, M. C. Asensio, J. Zhu, S. Zhou, Quasicrystalline 30° twisted bilayer graphene as an incommensurate superlattice with strong interlayer coupling, Proceedings of the National Academy of Sciences 115 (27) (2018) 6928–6933.

[13] E. J. Mele, Commensuration and interlayer coherence in twisted bilayer graphene, Physical Review B 81 (16) (2010) 161405.

[14] E. J. Mele, Interlayer coupling in rotationally faulted multilayer graphenes, Journal of Physics D: Applied Physics 45 (15) (2012) 154004.

[15] S. Talkington, E. J. Mele, Electric-field-tunable band gap in commensurate twisted bilayer graphene, Physical Review B 107 (4) (2023) L041408.

[16] S. Talkington, E. J. Mele, Terahertz circular dichroism in commensurate twisted bilayer graphene, Physical Review B 108 (8) (2023) 085421.

[17] M. Kindermann, Topological Crystalline Insulator Phase in Graphene Multilayers, Physical Review Letters 114 (22) (2015) 226802.

[18] E. Koren, I. Leven, E. Lörtscher, A. Knoll, O. Hod, U. Duerig, Coherent commensurate electronic states at the interface between misoriented graphene layers, Nature Nanotechnology 11 (9) (2016) 752–757.

[19] C. Riedl, C. Coletti, U. Starke, Structural and electronic properties of epitaxial graphene on SiC(0001): a review of growth, characterization, transfer doping and hydrogen intercalation, Journal of Physics D: Applied Physics 43 (37) (2010) 374009.

[20] I. Razado-Colambo, J. Avila, D. Vignaud, S. Godey, X. Wallart, D. P. Woodruff, M. C. Asensio, Structural determination of bilayer graphene on SiC(0001) using synchrotron radiation photoelectron diffraction, Scientific Reports 8 (1) (2018) 10190.

[21] K.-j. Kim, H. Lee, J.-H. Choi, Y.-S. Youn, J. Choi, H. Lee, T.-H. Kang, M. C. Jung, H. J. Shin, H.-J. Lee, S. Kim, B. Kim, Scanning Photoemission Microscopy of Graphene Sheets on SiO2, Advanced Materials 20 (19) (2008) 3589–3591.

[22] L. H. de Lima, A. de Siervo, R. Landers, G. A. Viana, A. M. B. Goncalves, R. G. Lacerda, P. Häberle, Atomic surface structure of graphene and its buffer layer on SiC(0001): A chemical-specific photoelectron diffraction approach, Physical Review B 87 (8) (2013) 081403.

[23] F. Matsui, R. Ishii, H. Matsuda, M. Morita, S. Kitagawa, T. Matsushita, S. Koh, H. Daimon, Characterizing Edge and Stacking Structures of Exfoliated Graphene by Photoelectron Diffraction, Japanese Journal of Applied Physics 52 (11R) (2013) 110110.

[24] S. Tricot, T. Jaouen, D. Sébilleau, P. Schieffer, Energy dependence of interference phenomena in the forward-scattering regime of photoelectron diffraction, Journal of Electron Spectroscopy and Related Phenomena 256 (2022) 147176.

[25] D. Sébilleau, R. Gunnella, Z.-Y. Wu, S. D. Matteo, C. R. Natoli, Multiple-scattering approach with complex potential in the interpretation of electron and photon spectroscopies, Journal of Physics: Condensed Matter 18 (9) (2006) R175.

[26] D. Sébilleau, C. Natoli, G. M. Gavaza, H. Zhao, F. Da Pieve, K. Hatada, MsSpec-1.0: A multiple scattering package for electron spectroscopies in material science, Computer Physics Communications 182 (12) (2011) 2567–2579.

[27] S. Tricot, D. Sébilleau, MsSpec package, Python version.

[28] L. Hedin, S. Lundqvist, Effects of Electron-Electron and Electron-Phonon Interactions on the One-Electron States of Solids, in: F. Seitz, D. Turnbull, H. Ehrenreich (Eds.), Solid State Physics, Vol. 23, Academic Press, 1970, pp. 1–181.

[29] L. Hedin, B. I. Lundqvist, Explicit local exchange-correlation potentials, Journal of Physics C: Solid State Physics 4 (14) (1971) 2064.

[30] T. Fujikawa, K. Hatada, L. Hedin, Self-consistent optical potential for atoms in solids at intermediate and high energies, Physical Review B 62 (9) (2000) 5387–5398.

[31] O. M. Küttel, R. G. Agostino, R. Fasel, J. Osterwalder, L. Schlapbach, X-ray photoelectron and Auger electron diffraction study of diamond and graphite surfaces, Surface Science 312 (1) (1994) 131–142.

[32] E. Maillard-Schaller, O. M. Kuettel, L. Schlapbach, X-ray photoelectron diffraction of the silicon–diamond interface, physica status solidi (a) 153 (2) (1996) 415–429.

[33] T. Greber, J. Wider, E. Wetli, J. Osterwalder, X-Ray Photoelectron Diffraction in the Backscattering Geometry: A Key to Adsorption Sites and Bond Lengths at Surfaces, Physical Review Letters 81 (8) (1998) 1654–1657.

[34] W. Auwärter, T. J. Kreutz, T. Greber, J. Osterwalder, XPD and STM investigation of hexagonal boron nitride on Ni(111), Surface Science 429 (1) (1999) 229–236.

[35] F. Matsui, T. Matsushita, H. Daimon, Photoelectron Diffraction and Holographic Reconstruction of Graphite, Journal of the Physical Society of Japan 81 (11) (2012) 114604.

[36] S. Roth, F. Matsui, T. Greber, J. Osterwalder, Chemical Vapor Deposition and Characterization of Aligned and Incommensurate Graphene / Hexagonal Boron Nitride Heterostack on Cu(111), Nano Letters 13 (6) (2013) 2668–2675.

[37] D. Agliz, A. Quémerais, D. Sébilleau, Splitting effects in high resolution and high energy photoelectron diffraction: the case of MgO(001), Surface Science 343 (1) (1995) 80–86.

[38] S. Juillaguet, L. Kubler, M. Diani, J. L. Bischoff, G. Gewinner, P. Wetzel, N. Bécourt, Strong element dependence of C 1s and Si 2p X-ray photoelectron diffraction profiles for identical C and Si local geometries in β-SiC, Surface Science 339 (3) (1995) 363–371.

[39] P. Schieffer, G. Jézéquel, B. Lépine, D. Sébilleau, G. Feuillet, B. Daudin, X-ray photoelectron diffraction from cubic GaN(001): an experimental and theoretical study, Surface Science 482-485 (2001) 593–599.

[40] J.-F. Sadoc, M. Impéror-Clerc, Some examples of quasiperiodic tilings obtained with a simple grid method, Europhysics Letters 144 (6) (2024) 66002.

[41] V. Fritzsche, D. P. Woodruff, Direct photoelectron-diffraction method for adsorbate structural determinations, Physical Review B 46 (24) (1992) 16128–16134.

[42] D. P. Woodruff, A. M. Bradshaw, Adsorbate structure determination on surfaces using photoelectron diffraction, Reports on Progress in Physics 57 (10) (1994) 1029.